

# Experimental and Numerical Study on the Damage Evolution Behaviour of Granitic Rock during Loading and Unloading

Dai Bing\*, Zhao Guoyan\*\*, H. Konietzky\*\*\*, and P. L. P. Wasantha\*\*\*\*

Received September 27, 2016/Accepted September 20, 2017/Published Online July 13, 2018

## Abstract

Theoretical and experimental studies have revealed that the damage evolution plays an important role in stability of rock structures. To investigate the damage characteristics of rocks during loading and unloading, a series of conventional triaxial tests and numerical simulations were conducted on granitic rock specimens under different confining pressures. The stress-strain characteristics and fracture patterns of tested specimens were first analyzed. It was found that the failure strain in unloading is smaller than the failure strain in loading. And the difference between the two strains is growing with increasing confining pressure. The failure patterns of specimens displayed two different failure mechanisms: a single distinct failure and a “X” failure. Based on the law of energy conservation, the energy evolution was analyzed. The results indicated that absorbed strain energy converted into elastic strain energy and dissipation energy. For evaluating and predicting damage, two damage degrees were proposed considering increase of dissipation energy and decrease of tangential modulus, respectively. The results show that before the reversal point of volumetric strain, the damage degrees were almost unchanged. During the process of unloading the damage degrees increases fast. For the same strain, lower confining pressure shows more damage. It indicates that the confining pressure has negative effects on increase of the damage degree. Then, the discrete element model based on elastic and unbreakable voronoi blocks was set-up for tri-axial tests. The energy evolution and damage process were simulated. And the ratio of failed contacts was used to simulate the damage degree. It shows that stress-strain behavior as well as micro- and macro-mechanical damage evolution can be reproduced by the DEM model.

Keywords: *triaxial test, loading and unloading, energy, damage degree, numerical simulation*

## 1. Introduction

Natural rock is commonly in the three-dimensional stress state. Rock excavations for various applications such as mining, caving and tunnelling disturb the original in-situ stress field. According to numerous previous studies in the literature, rock masses undergo loading before the excavation (Rellesmann *et al.*, 1957; Wahl *et al.*, 1997; Thasnanipan *et al.*, 1998; Ma *et al.*, 1999; Martino *et al.*, 2004). During and after the excavations rock masses close to the open rock surfaces of the excavation often undergo unloading and stress relaxation that can lead to severe rock failures, such as rock bursts, spalling and collapses (Wu *et al.* (1997), Ha *et al.* (1998)). The damage evolution in rocks during both loading and unloading is a non-equilibrium and nonlinear process and the origin and nature of damage evolution characteristics in rock can have significant differences for loading and unloading. Damage evolution behaviour directly influences the stability of rock structures, meaning that it is of

great importance for any kind of safety considerations of rock structures (Li *et al.*, 2014; Huang *et al.*, 2010).

Number of experimental studies has been conducted in the literature to understand the damage evolution behaviour of various rock types. Ayling *et al.* (1995) studied the microcrack propagation in two dry sandstones (Darley Dale and Gosford) during triaxial deformation and observed an initial closure of suitably oriented cracks followed by dilatant crack growth occurring predominantly parallel to the major loading axis. Baud and Meredith (1997) investigated the damage accumulation in Darley Dale sandstone during triaxial creep from pore volumetry and observed that the level of applied differential stress has a crucial effect on the creep rate and time-to-failure. Eberhardt *et al.* (1998, 1999) explored the progressive pre-peak damage process in pink Lac du Bonnet granite under uniaxial compression and showed that the crack initiation and crack damage thresholds for pink Lac du Bonnet granite are 39% and 75% of peak strength, respectively. Cai *et al.* (2004) studied the generalized crack

\*Ph.D., Nuclear Resources Engineering College, University of South China, Hengyang, China; Institut für Geotechnik, Technische Universität Bergakademie Freiberg, Germany; School of Resources and Safety Engineering, Central South University, Changsha, China (Corresponding Author, E-mail: daibingcsu@gmail.com)

\*\*Professor, School of Resources and Safety Engineering, Central South University, Changsha, China (E-mail: gy.z@263.net)

\*\*\*Professor, Institut Für Geotechnik, Technische Universität Bergakademie Freiberg, Germany (E-mail: konietzk@mailserver.tu-freiberg.de)

\*\*\*\*Lecturer, Institut Für Geotechnik, Technische Universität Bergakademie Freiberg, Germany (E-mail: wasanthaplp@gmail.com)

initiation and crack damage stress thresholds of granite under uniaxial compression, and found that the crack initiation and crack damage thresholds take a general form that is found to be applicable to jointed rock masses of fair or better quality by replacing the intact rock uniaxial compressive strength by the uniaxial compressive strength of the jointed rock mass. Sun *et al.* (2004) conducted a series of triaxial compression experiments on a weathered porphyrite and concluded that the tested weathered soft rock under both unsaturated and saturated conditions has strong confining-pressure dependency of deformation. Li *et al.* (2012) discussed the dispersion damage mechanics based on the fracture mechanics and established the relationship between the micro-fracture and the macro dilation. Wasantha *et al.* (2014) investigated the water-weakening behaviour of Hawkesbury sandstone in brittle regime and one of their observations suggests micro-cracking begins at progressively earlier stages of loading when confining stress increases. Shao *et al.* (2015) explored the effect of temperature on the thermo-mechanical behaviour of Australian Strathbogie granite under uniaxial compression and observed increasing temperature reduces the stress thresholds for crack initiation and crack damage and extends the duration of stable crack propagation.

The vast majority of the previous experimental studies considered the damage evolution of rocks under loading and only very few studies explored that under unloading scenario. For example, Guo *et al.* (2012) investigated the mechanical properties of Jintan mine rock salt under tri-axial unloading test and found that in the initial stage of unloading, the strain value has a linear relationship with confining pressure, axial and radial strains increase sharply with decreasing confining pressure. An obvious radial expansion is also shown during unloading confining pressure. Zhao *et al.* (2014) carried out true-triaxial unloading tests on granite specimens and found that the rock samples are prone to strain burst failure under a high unloading rate and the associated Acoustic Emission (AE) energy release in the strain burst process is dependent on the unloading rate. Wu *et al.* (2004) reported the deformation and strength characteristics of jointed red sandstone during the unloading of true-triaxial tests and proposed a new constitutive model which can reflect unloading failure characteristics of brittle-elastic rock masses. Zhang *et al.* (2010) and Qiu *et al.* (2010) studied the effect of unloading rate on the strength of rock and concluded that the strength of rock increases with increasing unloading rate.

Numerical methods, primarily the distinct element method (DEM)-based methods, have also been used in the literature to explore the damage evolution characteristics of rock. For example, Cundall (1980) Used Universal Distinct Element Code (UDEC) to simulate the behaviour of jointed rock masses subjected to high and transient loadings. Homand *et al.* (1998) used UDEC to reproduce most of the observable characteristics of damaged zone around an underground opening excavated into brittle rocks. Christianson (2006) also used UDEC to conduct numerical triaxial testing on simulated tuff samples to supplement existing uniaxial data. Gu *et al.* (2013) simulated unstable rock failure in

shear and compressive loading using UDEC and their results show that the failure stability is predominantly governed by the relative stiffness of failing discontinuities and loading stiffness of wall rocks. Tan *et al.* (2014, 2015) used UDEC to simulate the deformation process and failure behaviour of Mosel slate during the Brazilian tests and their results in better understanding of failure modes of Brazilian tests on foliated rocks and allow a more reliable interpretation of strength parameters. Chen *et al.* (2015, 2016) analysed the damage process of loaded brittle rocks using UDEC and found that reasonable stress–strain behaviour as well as micro- and macro-mechanical damage evolution can be reproduced by the presented DEM model. It should be noted that all the above numerical studies considered only the loading scenario.

Although the damage evolution behaviour of rock under loading has been well documented that of unloading has not been satisfactorily explored. Therefore, in this paper, we conduct a comprehensive experimental study and a DEM-based numerically simulation program to better understand the damage evolution characteristics of granitic rocks during loading and unloading. Based energy conservation theory, the process of energy conservation were analysed during the loading and unloading. The deformation behaviour of deformation modulus in loading and unloading were studied respectively. Two quantitative damage degrees defined by dissipation energy and the deformation modulus respectively are introduced to evaluate the evolution of damage in the loading and unloading process. At last, the UDEC model was used to simulate the damage evolution of rock under loading and unloading process.

## 2. Experimental Work

### 2.1 Testing Material and Sample Preparation

A granitic rock was used for the experiments. The granitic blocks were obtained at 400-600 m depth of San Shan Dao gold mine in Shan Dong province. Some basic material properties of the above granitic rocks is shown in Table 1. Cylindrical specimens with a diameter of 49-50 mm were cored from a single rock block, with all coring performed in a common orientation. The cylindrical cores were then cut to a length of 110 mm. Rock cores did not show any visible discontinuities, meaning that they can be assumed as macroscopically homogeneous. Then, the end surfaces of each specimen were ground to ensure the ends were perfectly flat and perpendicular to the long axis of the samples and the final length of the specimens varied between 99.5 and 100 mm (length-to-diameter ratio  $\approx 2$ ). The machining accuracy

Table1. Basic Properties of the Tested Material

Property	Mean value	Range
Longitudinal wave velocity (m/s)	3500	3200-3800
Density (kg/m <sup>3</sup> )	2500	2470-2542
Compressive strength dry (MPa)	131	119.3-138.2
Elastic Modulus (GPa)	52	50.81-53.12
Poisson's ratio	0.17	0.15-0.19

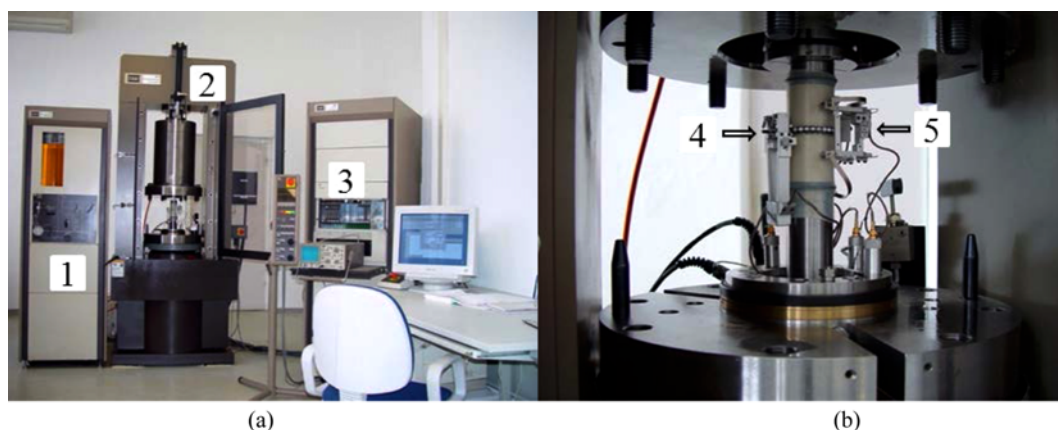


Fig. 1. Components of the Testing Apparatus: (a) Overall View of the MTS 815 Rock Testing System, (b) Arrangement of the Specimen Within the Triaxial Cell (1: pump unit, 2: loading frame, 3: data acquisition unit, 4: an circumferential LVDT, 5: an axial LVDT)

of the specimens was in accord with the specifications of International Society for Rock Mechanics (ISRM) recommended methods (Ulusay *et al.*, 2007).

## 2.2 Testing Apparatus and Procedure

We conducted both loading and unloading tests under triaxial stress conditions using MTS 815 rock testing system (Fig.1). This servo-controlled testing system has five major units (Fig. 1); (1) pumping unit for applying the confining pressure and this unit has a capacity of 40 MPa, (2) loading frame with a capacity of 3600 KN for applying the axial load, (3) data acquisition unit for recording the data related to pressure and loading, (4) linear variable differential transducer (LVDT) unit to measure the circumferential strain and (5) a separate LVDT unit to measure the axial strain.

The testing program was conducted in two series – conventional loading tests on one set of specimens and unloading tests on the other specimen set – under three different confining pressures –  $\sigma_2 = \sigma_3 = 10, 20$  and  $30$  MPa. In case of the loading tests, the confining

pressure was first applied to the desired level before the constant stress rate axial loading is applied at a rate of  $0.05$  MPa/s (provide hydrostatic pressure as much as possible) until failure (see Fig. 2).

For unloading tests, the confining pressure was first applied similar to the loading tests and set to a pre-determined level (i.e.  $10, 20,$  and  $30$  MPa). Then the axial load was applied at a constant strain rate of  $0.05$  MPa/s until the deviatoric stress reaches  $80\%$  (close to the yield strength and greater than the uniaxial strength) of the peak strength under a given confining pressure (the peak strengths under different confining pressures were determined from the loading tests). The unloading process (releasing the confining pressure while maintaining a constant axial stress) was started after that at a rate of  $0.05$  MPa/s and continued until the specimen failure (see Fig. 2).

## 3. Experimental Results and Analysis

The results of the experimental work performed as described in the previous section were analysed in different ways to meaningfully describe the damage evolution characteristics of the tested granitic rock under loading and unloading.

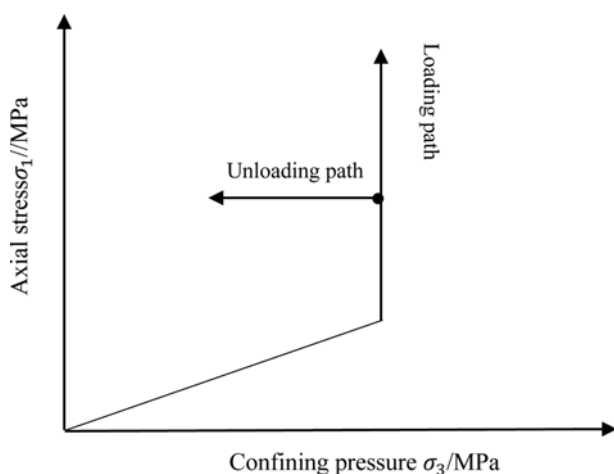


Fig. 2. Schematic Diagram of the Stress Path for Loading and Unloading Tests

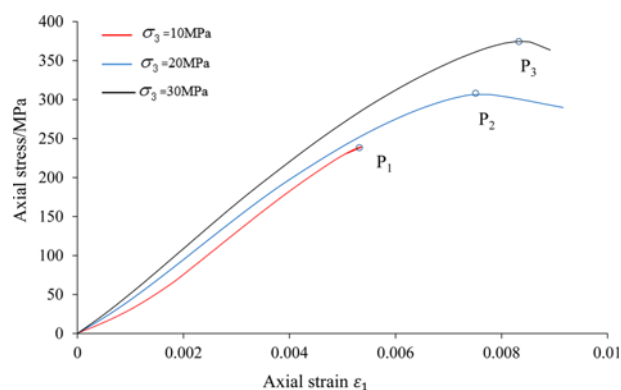


Fig. 3. The Stress–strain Curves of Specimens in Conventional Tri-axial Compression Tests

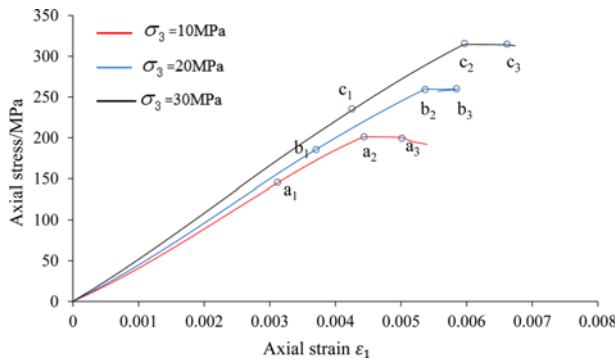


Fig. 4. The Stress-strain Curves of Specimens Under Different Confining Pressures in Loading And Unloading

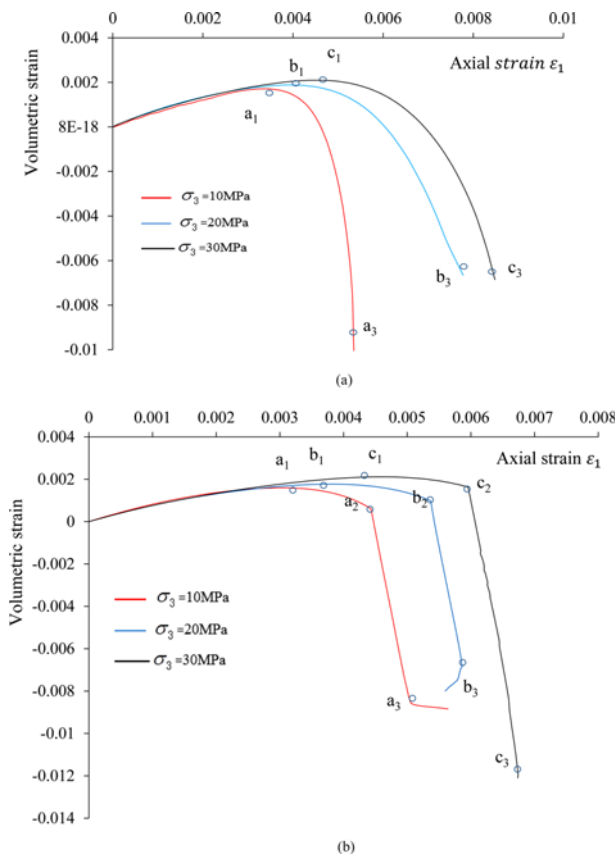


Fig. 5. Volumetric Strain Versus Axial Strain of Specimens: (a) Loading Test, (b) Unloading Test

### 3.1 Stress-strain Characteristics and Failure Mechanisms

Figure 3 shows the stress-strain curves of the specimens tested under loading. The points  $P_1$ ,  $P_2$  and  $P_3$  on Fig. 3 indicate the peak strengths ( $\sigma_{3c}$ ) for specimens tested under the confining

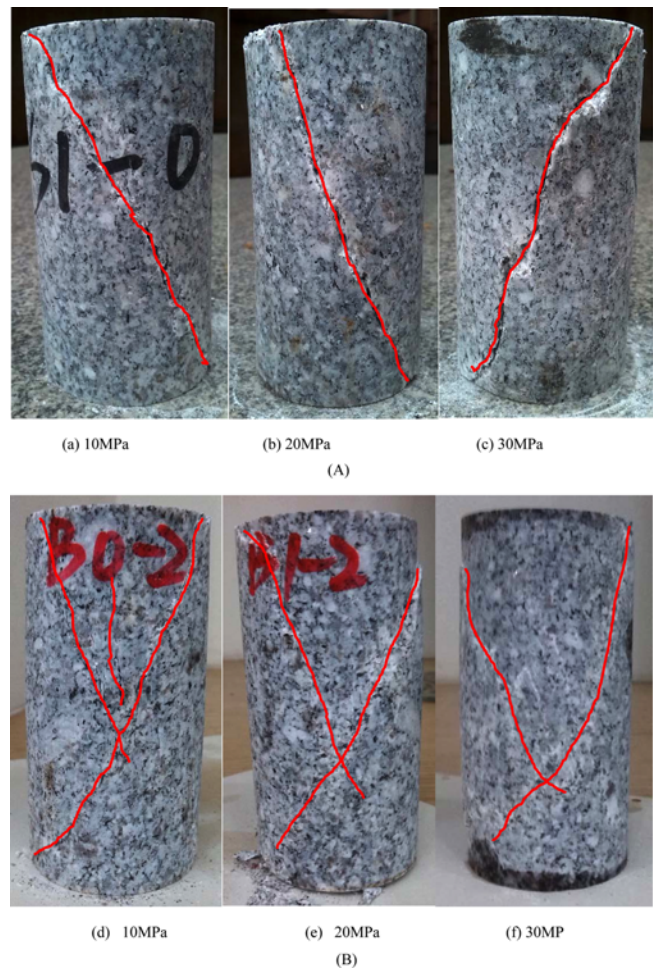


Fig. 6. Failed Granite Samples at Different Confining Pressure: (A) Conventional Tri-axial Compression Tests, (B) Tri-axial Tests in Loading and Unloading

pressures of 10, 20 and 30 MPa, respectively. The stress-strain curves of the specimens tested for unloading are shown in Fig. 4. As described before, the specimens were loaded up to 80% of their peak strengths before the unloading process started. The points  $a_2$ ,  $b_2$  and  $c_2$  of Fig. 4 indicate the beginning of unloading and the points  $a_3$ ,  $b_3$  and  $c_3$  indicate the end of unloading process at confining pressures of 10, 20 and 30 MPa, respectively. The volumetric strain  $\varepsilon_v$  ( $\varepsilon_v = \varepsilon_1 + 2\varepsilon_3$ ) versus axial strain relationships are shown in Fig. 5. The points  $a_1$ ,  $b_1$  and  $c_1$  of Fig. 5 correspond to the reversal points of volumetric strain versus axial strain curves of Fig. 5 for the confining pressures of 10, 20 and 30 MPa, respectively. Table 2 summarizes the important mechanical observations obtained from stress strain variations of Figs. 2, 3

Table 2. The Stress States of Points

$\sigma_3$ /MPa	$\sigma_{3c}$ /MPa	$\sigma_f$ /MPa	$\sigma_f$ /MPa	$\sigma_f/\sigma_{3c}$	$\sigma_f/\sigma_{3c}$	Failure strain in loading	Failure strain in unloading
10	237	150	190	63.3%	80%	0.0058	0.0051
20	306	200	245	65.4%	80%	0.0075	0.0058
30	362	250	290	69.1%	80%	0.0085	0.0066

Table 3. Fitting Results for  $E_T$  in Loading and Unloading

Parameters	Loading by Eq. (2)			Parameters	Unloading by Eq. (3)		
	10	20	30		10	20	30
$B_4$	53.736	55.490	58.550	$C_4$	3.049	44.738	47.599
$B_1$	-0.002	-0.553	-0.267	$C_1$	-5.210	-5.634	-7.991
$B_2$	25.410	70.840	72.283	$C_2$	-0.815	-1.571	-2.481
$B_3$	0	0	0	$C_3$	3.523	9.315	13.844
$R^2$	0.970	0.968	0.975	$R^2$	0.966	0.954	0.983

and 5 (in Table 2,  $\sigma_i$  represents the axial stress at which the volumetric strain curve reverses ( $i = a_1, b_1, c_1$ ) and  $\sigma_j$  represents the axial stress at which the unloading was started ( $j = a_2, b_2, c_2$ )). Table 2 clearly shows that  $\sigma_i$  increases with increasing of confining pressure in loading and unloading. The ratio of  $\sigma_i/\sigma_{3c}$  also rises with increasing of confining pressure according to Table 2 and it is within the range of 60%-70% of peak strength for the considered range of confining pressures. These behaviours are akin to those observed by Lajtai (1985), Bieniawski (1967) and Eberhardt (1999). Moreover, Table 2 depicts that the failure strain for unloading is smaller than that for loading under all three confining pressures and the difference becomes more pronounced with increasing confining pressure.

Post-failure images of the tested specimens are shown in Fig. 6. Two distinct failure patterns can be observed from these images for the specimens tested under loading and unloading – the specimens tested under loading failed predominantly with a single shear fracture plane and two intersecting shear fracture planes are evident from the samples tested for unloading.

### 3.2 The Evolution of Secant Modulus

To describe the variation of secant modulus  $E_T$  (it was calculated from two data points which are close to each other in curve of axial stress versus axial strain) with the axial stress and confining pressure, an exponential function is shown as following (Chen *et al.*, 2016; Peng *et al.*, 2015):

$$E_T = A_1 \exp\left(\frac{\sigma_1 + A_3 \sigma_3}{A_2}\right) + A_4 \quad (1)$$

Where  $A_1, A_2, A_3$  and  $A_4$  are fitting constants.

We can see from Fig. 7 in loading tests the secant modulus became stable over a range of the axial stress when the confining pressure is constant, and then decreases with increasing axial stress. This shows that the variation of secant modulus is due to changing axial stress. In this process due to constant of confining pressure,  $A_3 \sigma_3$  is constant. So in loading test the Eq. (1) can be given as follows:

$$E_T = B_1 \exp\left(\frac{\sigma_1 + B_3}{B_2}\right) + B_4 \quad (2)$$

Where  $B_1, B_2, B_3$  and  $B_4$  are fitting constants.

During the process of unloading the secant modulus decreased with confining pressure decreases gradually when the axial is constant in Fig. 8. It shows that the confining pressure has great influence on the secant modulus than axial stress during the

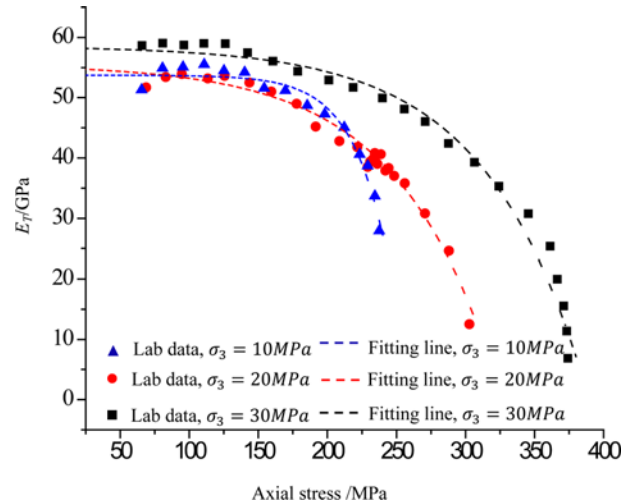


Fig. 7. Fitting and Experimental Results: the Deformation Modulus Versus Axial Stress in Loading Tests

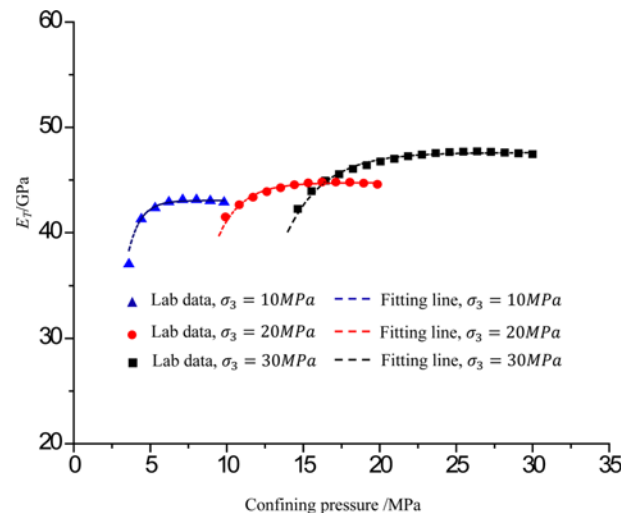


Fig. 8. Fitting and Experimental Results: the Deformation Modulus Versus Confining Pressure in Unloading Stage of Unloading Tests

process of unloading. So in process of unloading the Eq. (1) can be shown as follows:

$$E_T = C_1 \exp\left(\frac{\sigma_3 + C_3}{C_2}\right) + C_4 \quad (3)$$

Where  $C_1, C_2, C_3$  and  $C_4$  are fitting constants.

Fitting results obtained by Eq. (2) and (3) are shown in Table 3.  $R^2$  is the coefficient of correlation.

Fitting and experimental results for the secant modulus  $E_T$  are shown in Fig. 7 and Fig. 8.

When the axial stress is relatively low, the secant modulus increases with increasing axial stress (This part of curve is not shown in Fig. 7). This may result in the crack closure. After the reversal of volumetric strain the secant modulus decreases which was as a result of damage accumulating to critical value. The critical value of damage for secant modulus increases with increasing confining pressures. It also can be observed from the Fig. 8 in the initial stage of unloading the secant modulus decreases slowly, and finally decreases rapidly near the end of

unloading process at confining pressures of 10, 20 and 30 MPa, respectively which reflects the cumulative damage in the rock.

### 3.3 Energy Evolutions in the Process of Loading and Unloading

In triaxial tests of rocks, test machine does positive work to the specimen in the axial direction; confining pressure does negative work, due to the radial dilation of the specimen. So the strain energy  $U$  of rock in the whole process of tri-axial tests can be expressed as follow (Huang *et al.*, 2014; Dai *et al.*, 2015; Chen *et al.*, 2016):

$$U = U_1 + U_3 \tag{4}$$

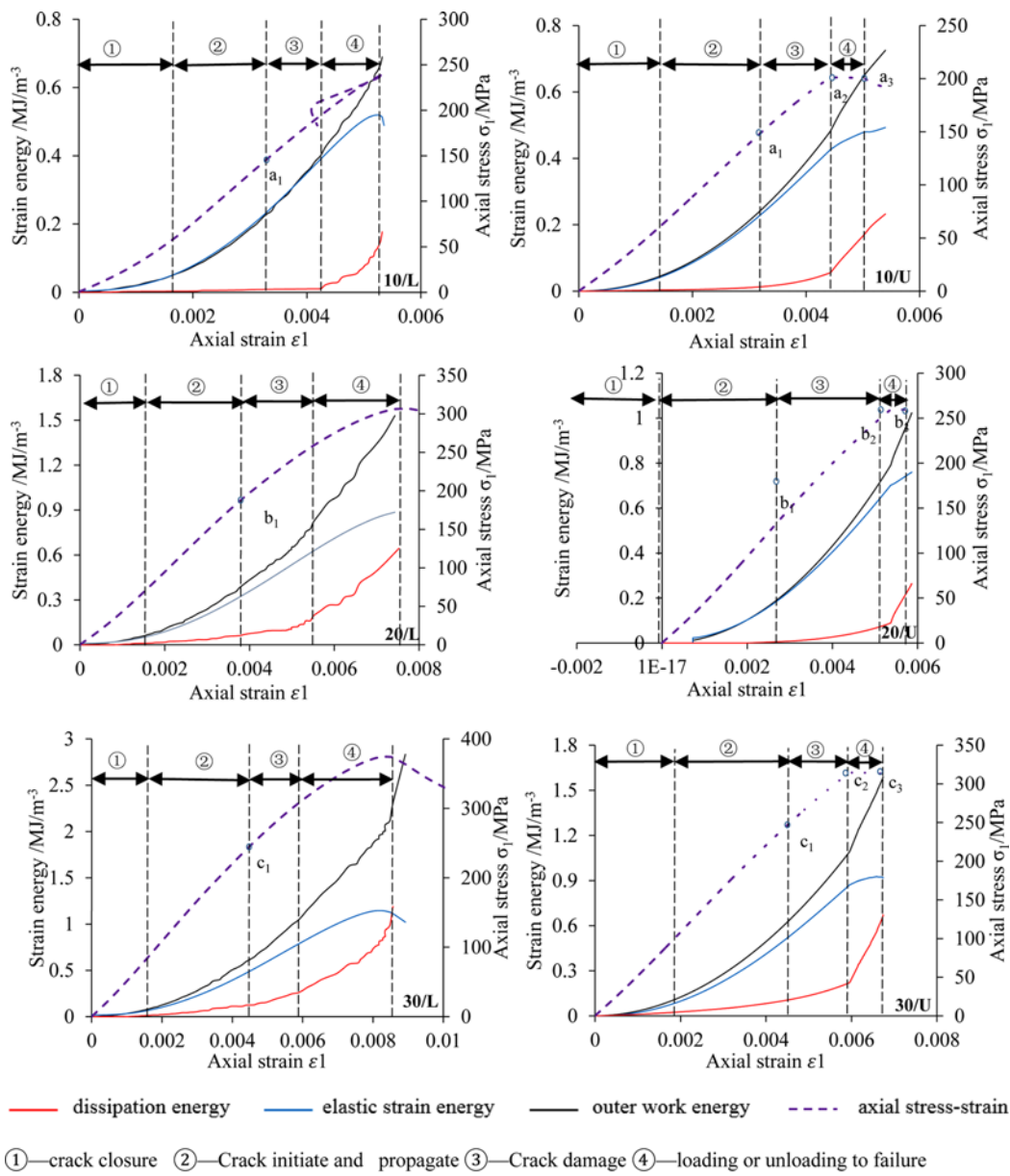


Fig. 9. Energy in Loading and Unloading Tests for Specimens: Outer Work Energy Versus Axial Strain, Elastic Strain Energy Versus Axial Strain, Dissipation Energy Versus Axial Strain

$$U_1 = \int_0^{\epsilon_1^t} \sigma_1 d\epsilon_1 \tag{5}$$

$$U_3 = 2 \int_0^{\epsilon_3^t} \sigma_3 d\epsilon_3 \tag{6}$$

Where,  $\epsilon_1^t$  and  $\epsilon_3^t$  are the axial and lateral strain at any time t, respectively.

Based on the principium of energy conservation, the total strain energy  $U$  can be divided into two parts, the elastic strain energy  $U_e$  which is stored in specimens, and the plastic-damage strain energy  $U_d$  which is responsible for plastic deformation and crack propagation in specimens. That is,

$$U = U_e + U_d \tag{7}$$

According to Xie (2005, 2008) and Huang (2014) the elastic strain energy is given by:

$$U_e = \frac{1}{2} \sigma_1 \epsilon_1^e + \frac{1}{2} \sigma_2 \epsilon_2^e + \frac{1}{2} \sigma_3 \epsilon_3^e = \frac{1}{2E} [\sigma_1^2 + 2(1-\nu)\sigma_3^2 - 4\nu\sigma_1\sigma_3] \tag{8}$$

Substituting Eq. (4)-(6) (8) into Eq. (7), the following equation is obtained:

$$\int_0^{\epsilon_1} \sigma_1 d\epsilon_1 + 2 \int_0^{\epsilon_3} \sigma_3 d\epsilon_3 = \frac{1}{2E} [\sigma_1^2 + 2(1-\nu)\sigma_3^2 - 4\nu\sigma_1\sigma_3] + U_d \tag{9}$$

The calculated energy according to Eq. (8) and Eq. (9) for loading and unloading tests are shown in Fig. 9 and Table 4.

According to Fig. 9  $U$ ,  $U_e$  and  $U_d$  understandably increase with increasing axial strain. Before the reversal of the volumetric strain curve (i.e. points  $a_1, b_1, c_1$  of the curves) total energy,  $U$  comprises mainly by the elastic energy,  $U_e$  with relatively insignificant contribution from dissipation energy,  $U_d$  for both loading and unloading tests under all confining pressures. From the reversal of volumetric strain curve dissipation energy,  $U_d$  gradually increases until the failure for loading tests under all confining pressures. In contrast, it gradually increases from reversal point of the volumetric strain curve until the unloading begins for unloading tests followed by a rapid increase until the failure under all confining pressures (contrasting gradients can be seen from the curves of Fig. 9 before and after unloading begins for unloading tests). This indicates that unloading of loaded rocks fail with relatively lower axial strain increase compared to rocks that fail by pure loading, which is also mentioned in last chapter shown in Table 2.

Dissipation energy variations of Table 4 also shows that the total energy dissipation at rock failure are 0.18, 0.60 and 0.8 MJ/m<sup>3</sup> for loading tests and are 0.13, 0.25 and 0.6 MJ/m<sup>3</sup> for unloading test under 10, 20 and 30 MPa confining pressures, respectively. This reveals that although the failure occurs with less axial strain increase unloading failures of rock dissipate lower amount of energy compared to those fail by pure loading.

Table 4. The Energy at Key Points in Loading and Unloading Tests

The key point	Confining pressure	Loading test			Unloading test		
		U/ MJ/m <sup>3</sup>	U <sub>e</sub> /MJ/m <sup>3</sup>	U <sub>d</sub> /MJ/m <sup>3</sup>	U /MJ/m <sup>3</sup>	U <sub>e</sub> /MJ/m <sup>3</sup>	U <sub>d</sub> /MJ/m <sup>3</sup>
a <sub>1</sub>	10MPa	0.21	0.20	0.01	0.22	0.21	0.01
b <sub>1</sub>	20MPa	0.35	0.31	0.04	0.38	0.36	0.02
c <sub>1</sub>	30MPa	0.58	0.41	0.17	0.59	0.45	0.14
a <sub>2</sub>	10MPa	0.44	0.41	0.03	0.47	0.41	0.06
b <sub>2</sub>	20MPa	0.72	0.58	0.14	0.76	0.68	0.08
c <sub>2</sub>	30MPa	1.0	0.75	0.25	1.05	0.85	0.20
a <sub>3</sub>	10MPa	0.68	0.5	0.18	0.62	0.49	0.13
b <sub>3</sub>	20MPa	1.45	0.85	0.60	0.10	0.75	0.25
c <sub>3</sub>	30MPa	1.90	1.10	0.80	1.52	0.92	0.60

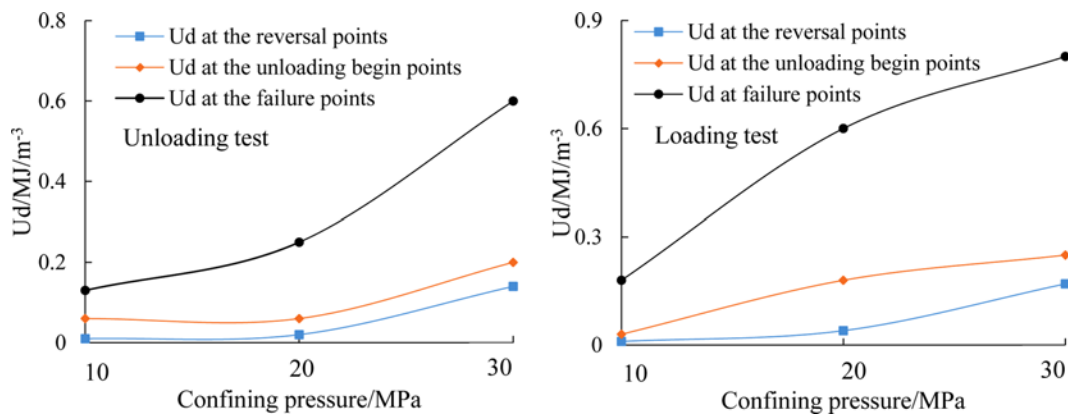


Fig. 10. Dissipation Energy Versus Confining Pressure at Different Points

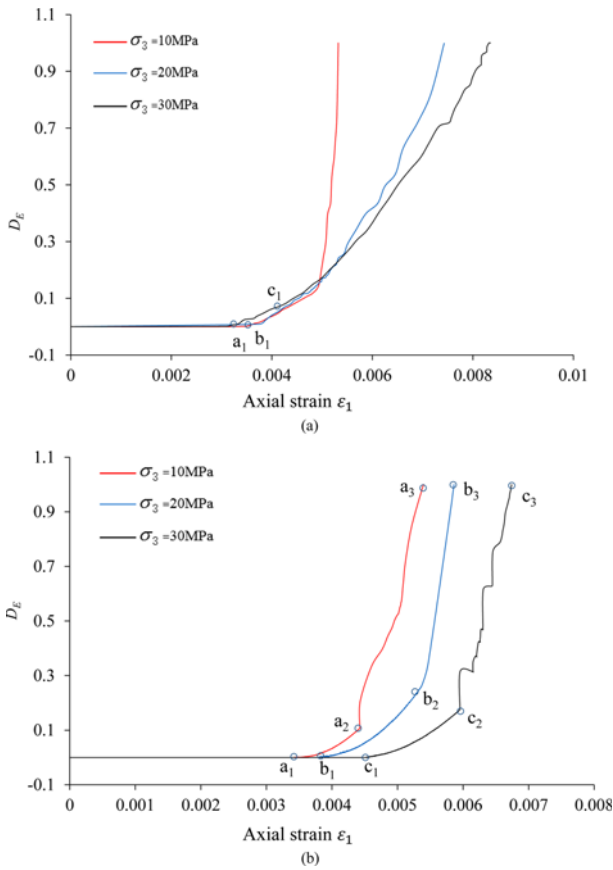


Fig. 11. Damage Degree  $D_E$  Versus Axial Strain: (a) Loading Test, (b) Unloading Test

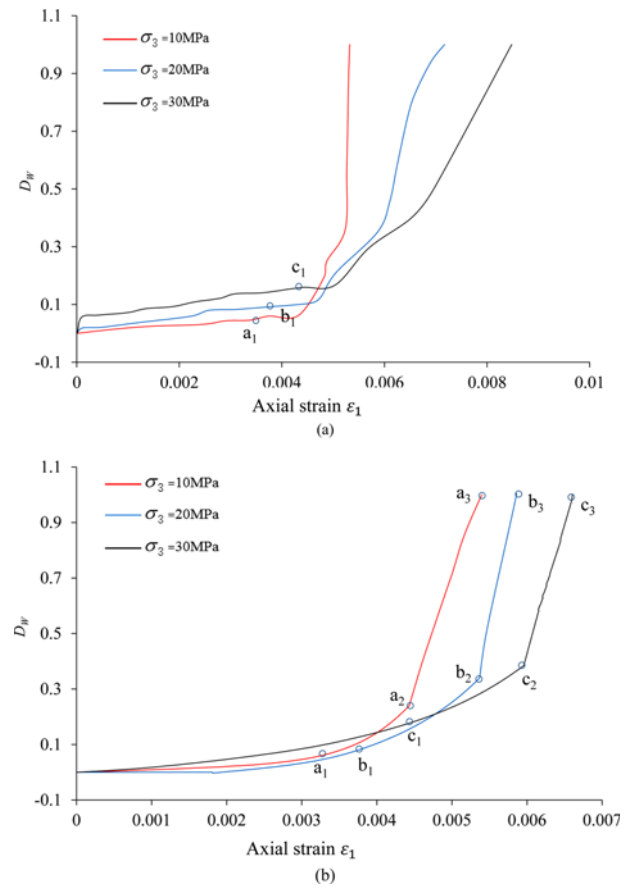


Fig. 12. Damage Degree  $D_W$  Versus Axial Strain: (a) Loading Test, (b) Unloading Test

Compare the energy conversions under different confining pressures in loading and unloading as shown in Fig. 10 and Table 4, it can see that the dissipation energy  $U_d$  increases with increasing confining pressure. And the rates of the dissipation energy  $U_d$  also increases with increasing confining pressure in unloading test which is faster than that in loading test as shown in Fig. 10.

### 3.4 The Damage Evolution Based on Secant Modulus and Dissipation Energy

In order to characterize the damage evolution, dissipation energy and secant modulus are used to evaluate the damage evolution under loading and unloading. These damage degrees are defined as follows (Zhao *et al.*, 2105; Chen *et al.*, 2016):

$$D_W = \frac{U_D}{U_{D_{max}}} \quad (10)$$

$$D_E = \frac{E_{T_0} - E_T}{E_{T_0} - E_{T_1}} \quad (11)$$

Where  $U_{D_{max}}$  is the dissipation energy at the end of unloading.  $E_{T_0}$  is the secant modulus at the reversal of volumetric strain.  $E_{T_1}$  is the secant modulus at the end of unloading.

The evolution of damage degrees in unloading tests are shown in Fig. 11(b) and Fig. 12(b). For comparative analysis the evolution of that in loading tests are also shown in Fig. 11(a) and Fig. 12(a).

Figure 12 clearly shows that  $D_W$  increases slowly before the reversal of volumetric strain at which  $D_W$  is 0.052, 0.084 and 0.174 in unloading test (Fig. 12(b)) and  $D_W$  is 0.05, 0.08 and 0.12 in loading test (Fig. 12(a)) under the confining pressures of 10, 20 and 30 MPa, respectively. And  $D_E$  almost unchanged in this process as shown in Fig. 11. It indicated that the work done by outer forces mainly converted in elastic energy stored in rock. From the reversal of volumetric strain to the start of unloading,  $D_W$  and  $D_E$  increase fast. At this time,  $D_W$  is 0.233, 0.343 and 0.371.  $D_E$  is 0.103, 0.244 and 0.315. It indicated that the reversal point of volumetric strain is a point of damage acceleration in loading stage. And it can be observed from the Fig. 11 and Fig. 12 that the damage of the acceleration point increases with increasing confining pressure. During the process of unloading  $D_W$  increases faster. The average variations of  $D_W$  and  $D_E$  in unloading are 0.69 and 0.78, respectively. About 70%-80% of damage happened in this stage.

In addition, for the same strain, lower confining pressure shows more damage. Compare the damage degrees under loading and



unloading in Fig. 11(a)-(b) & Fig. 12(a)-(b), the damage degrees in unloading test is faster than that in loading test under the same confining pressures and the difference becomes more pronounced with increasing confining pressure. If we neglect the variation before the reversal of volumetric strain,  $D_W$  and  $D_E$  show a similar change laws. This indicates that both are good to predict the evolution of damage for different confining pressures under loading and unloading.

### 4. Numerical Simulation

#### 4.1 Numerical Simulation Procedure

Universal Distinct Element Code (UDEC) was used for the numerical simulations. UDEC is a two-dimensional numerical program based on the distinct element method. UDEC especially joint model used in UDEC captures several features that are representative of the physical response of joints. For joint model in UDEC, all blocks are connection with contacts (corner-to-corner contacts, edge-to-corner contacts and edge-to-edge contact). However, edge-to-edge contact is important, because it corresponds to the case of a rock joint closed along its entire length. The tensile and shear stresses that act on the contacts are calculated. If the maximum tensile stress exceeds the tensile strength of the contacts or the maximum shear stress exceeds the shear strength of the contacts, the contacts will break. And a micro-tensile crack or a micro-shear crack, respectively, will form. To investigate the evolution of damage under both loading and unloading scenarios, the UDEC model was set-up with elastic but indivisible voronoi

blocks. Model size was akin to those of the diametrical cross section of specimens used for laboratory testing (i.e. 50 mm width and 100 mm height) and the average edge length of voronoi blocks was selected as 0.0025 m which yielded about 840 voronoi blocks in total within the model. Fig. 13 shows a typical UDEC model and how individual voronoi blocks are numerically interconnected.

For a distinct element model such as the UDEC that synthesizes macro-scale material behaviour from the interactions of micro-scale components, the input properties of the microscopic constituents are usually not known. Such intrinsic characteristics imply that it is nearly impossible to calibrate a set of macro output properties from the assembly such that they are exactly equal to that of the physical tests. Only a set of comparable properties can be obtained from the calibrated model. The basic geo-mechanical properties of the testing material as depicted in Table 1 were used as input parameters for the numerical model and further input parameters used are tabulated in Table 5. The stresses for numerical simulation of both loading and unloading tests were applied exactly similar to the way they were applied during laboratory testing. In the present numerical study, specimens are loaded under a uniaxial vertical compression in a velocity controlled manner. A sufficiently low loading rate of 0.03 m/s is applied to ensure that the specimen remains in a quasi-static equilibrium throughout the test. It takes approximately 1000,000 steps to load one specimen to complete failure. Besides, in UDEC model, the axial stress is calculated using the average stress in the y direction at dozens of locations in the top area. The lateral and axial strains (strain is equal to displacement divided by the length or width of model) are calculated using the average displacement in the x and y directions at dozens of locations in some sampling area to monitor the specimen response.

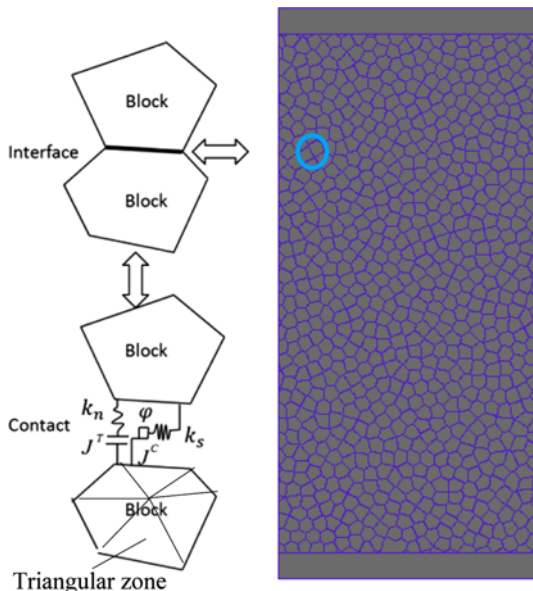


Fig.13. UDEC Model

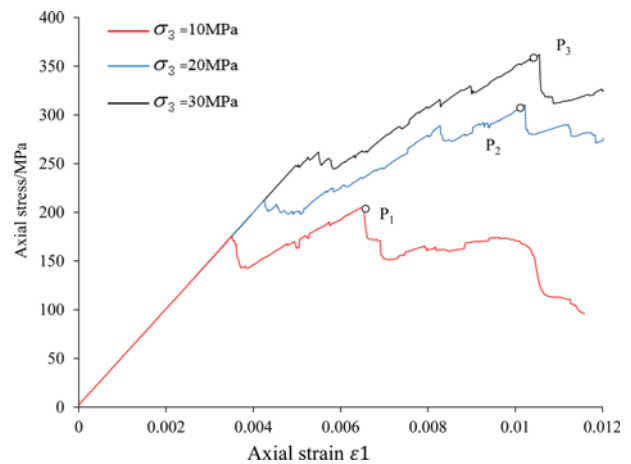


Fig. 14. Simulation Results of Tri-axial Loading Tests

Table 5. UDEC Parameters for Specimens

Parameters	$k_n(\text{Pa/m})$	$k_s(\text{Pa/m})$	$J^i(\text{MPa})$	$J_r(\text{MPa})$	$J^c$	$J_r^c$	$\Phi(^{\circ})$	$\Phi_r(^{\circ})$
Model	5e14	5e14	30	0	40	0	38	5

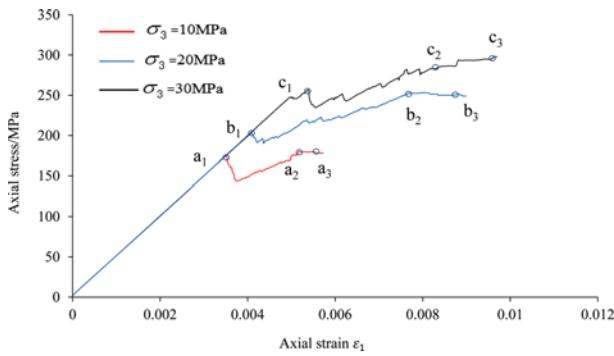


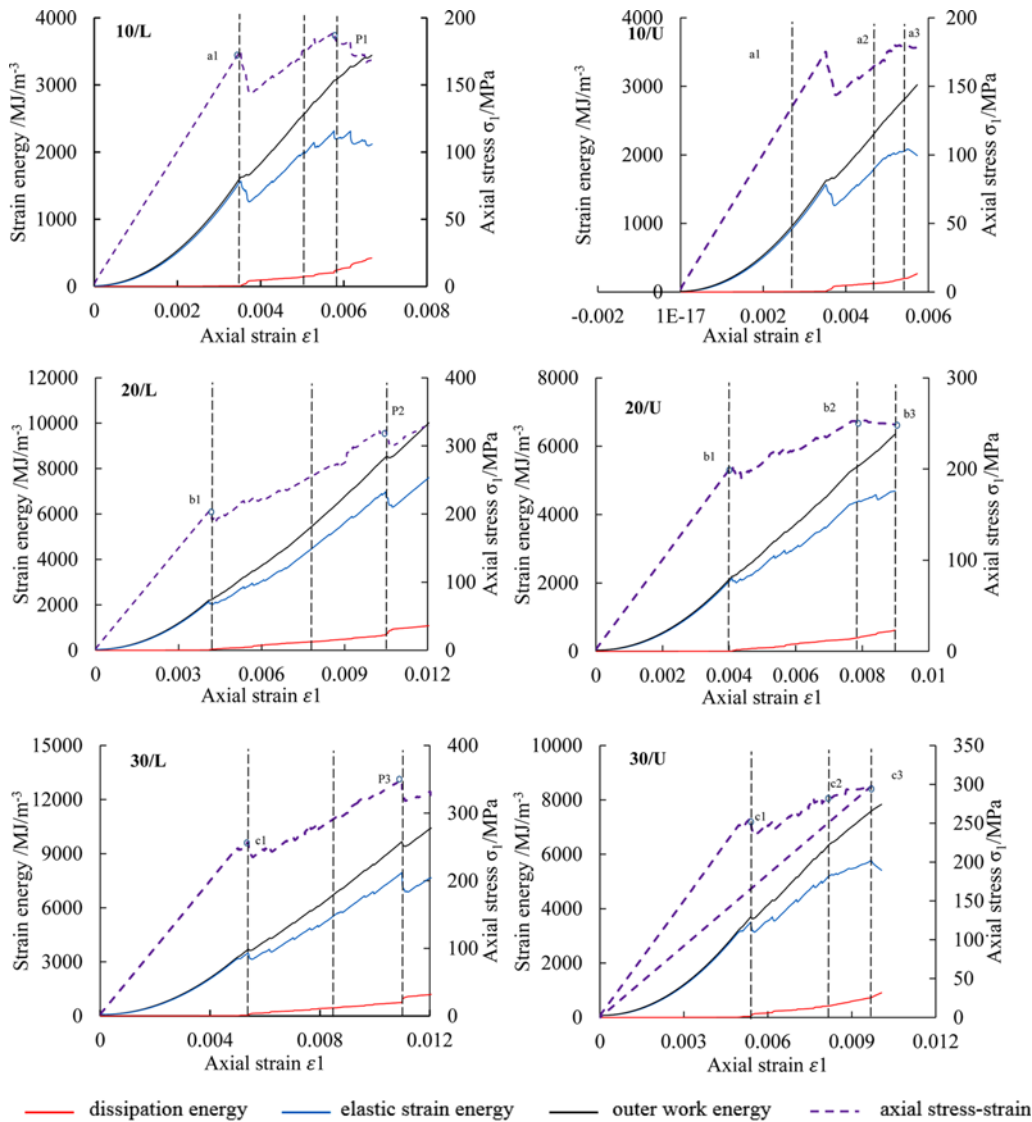
Fig. 15. Simulation Results of Tri-axial Unloading Tests

#### 4.2 Simulate the Stress-strain Characteristics

To simulate unloading process, we must know the stress-strain curves of rock under different confining pressures in loading.

Fig. 14 shows the curves of axial stress versus axial strain of rock under different confining pressures in loading tests. The peak load is 210 MPa, 305 MPa and 365 MPa under confining pressure of 10, 20 30 MPa respectively. Compared with lab test results, the corresponding absolute values have relative error of 13.5%, 0.3% and 1.1%, respectively. The elastic modulus and poissons rate of the numerical model are 52 GPa and 0.18 which gives compared to the lab result a relative error of 4% and 5.9%.

Figure 15 shows the curves of axial stress versus axial strain of rock under different confining pressures in unloading tests. As described before, the points a<sub>2</sub>, b<sub>2</sub> and c<sub>2</sub> of Fig. 15 indicate the beginning of unloading and the points a<sub>3</sub>, b<sub>3</sub> and c<sub>3</sub> indicate the end of unloading process at confining pressures of 10, 20 and 30 MPa, respectively. The points a<sub>1</sub>, b<sub>1</sub> and c<sub>1</sub> indicate the reversal of volumetric strain. The axial stresses at the reversal of volumetric strain are 170 MPa, 210 MPa and 248 MPa at confining



10/L, 10/U: “10” means confining pressure of 10MPa, “L” means loading test, “U” means unloading test.

Fig. 16. Energy in Numerical Simulation for Specimens Under Different Confining Pressures: Outer Work Energy Versus Axial Strain, Elastic Strain Energy Versus Axial Strain, Dissipation Energy Versus Axial Strain

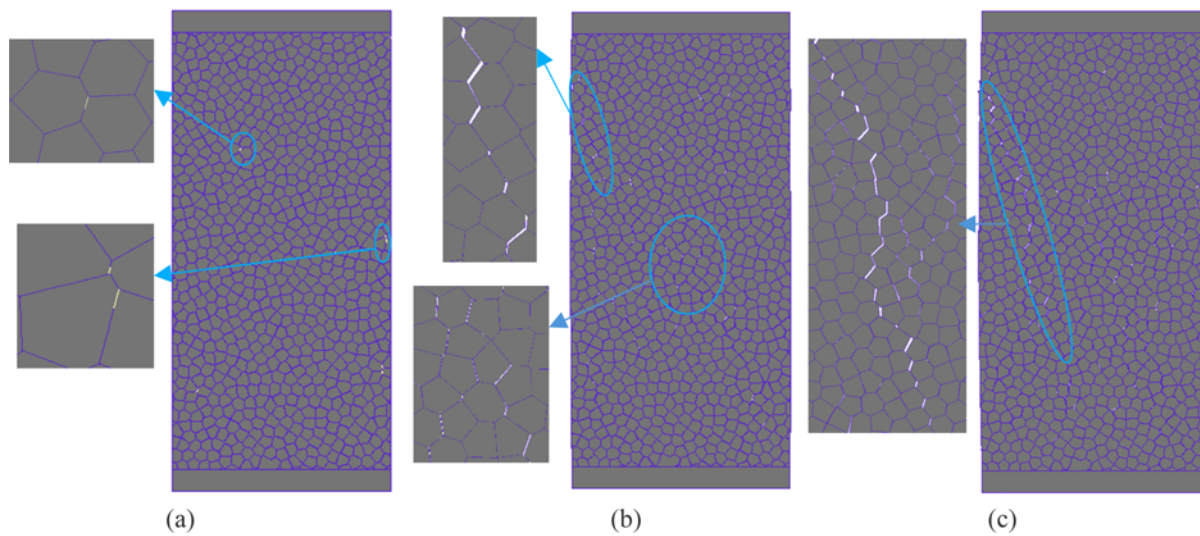


Fig. 17. The Damage Process in Tri-axial Test for Confining Pressure of 10 MPa: (a) Before Reversal of Volumetric Strain, (b) At Reversal of Volumetric Strain, (c) Near the Peak Point

pressures of 10, 20 and 30 MPa, respectively. Their values are 80.1%, 68.8% and 67.9% of peak strengths at confining pressures of 10, 20 and 30 MPa, respectively. The average value of them is 72.2%, which is similar to the results of lab tests. After the reversal of volumetric strain, the axial stress nonlinearly increased. This means that the macro cracks are formed and propagated. In addition, the variation of axial strain in unloading increases with increasing confining pressures.

#### 4.3 Simulate the Evolution of Damage Process in Loading and Unloading

In order to better describe the damage process, the energy features in UDEC are taken into account. In UDEC, the total energy balance can be expressed in terms of the released energy ( $W_r$ ), which is the difference between the work done at the boundary of the model and the total stored and dissipated strain energies:

$$W_r = W - (U_c + U_b + W_j + W_p) \quad (12)$$

Where  $U_c$  = Total stored strain energy in material  
 $U_b$  = Total change in potential energy of the system  
 $W$  = Total out work energy supplied to the system  
 $W_j$  = Total dissipated energy in joint shear  
 $W_p$  = Total dissipated work in plastic deformation of intact rock  
 $W_r$  = Released energy

In this paper, only total work energy ( $W$ ), total stored strain energy ( $U_c$ ) and total dissipated The energy features and damage features in loading and unloading at confining pressures of 10, 20 and 30 MPa, respectively are shown in Fig. 16 and Fig. 17.

As shown in Fig. 16 all energy features can be divided into three stages. Before the point of  $a_1$  or  $b_1$  or  $c_1$ , the out work energy ( $W$ ) almost converted to material strain energy ( $U_c$ ). The

dissipated energy ( $W_j$ ) almost unchanged. Only a few micro-cracks initiated. As the axial stress reached peak point ( $P_1, P_2, P_3$ ), the dissipated energy ( $W_j$ ) increased steadily with increasing axial strain in this stage and micro-cracks penetrated into notable macro-crack (see Fig. 17). After the peak point, the model failed (see Table 6). The material strain energy ( $U_c$ ) decreased and the dissipate energy increased fast.

Compare the curves of strain energy in loading and unloading in Fig. 16. It clearly shows that the out work energy, material energy and dissipated energy in unloading are smaller than that in loading when the model failed. It demonstrated the model in unloading is easier damage than that in loading. In addition, the all of strain energies in loading and unloading increased with confining pressures increased. It indicates that the confining pressure has negative effects on the granite damage.

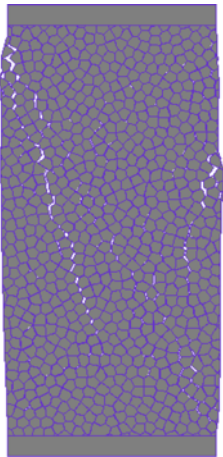
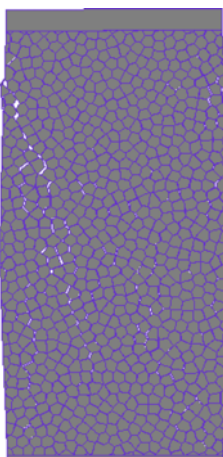
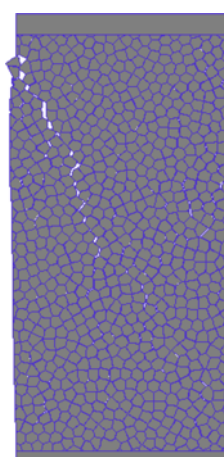
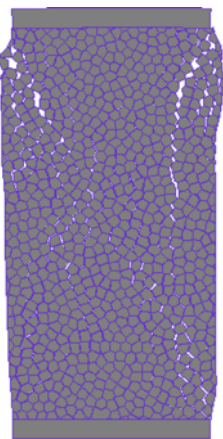
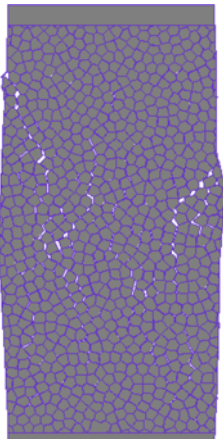
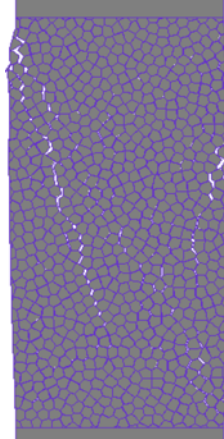
A stress drop is obviously observed in Fig. 16. This is due to micro-cracks penetrated into macro-crack (see Fig. 17), which led to the material strain energy start decreased and dissipated energy increased. It indicated that the stress of this point is the damage crack stress. Meanwhile, the damage crack stress increased with confining pressures increased.

Table 6 shows the damage pattern of rock under different confining pressures in loading and unloading. Both numerical simulations and lab tests demonstrate the shear failure mechanism (a single distinct failure or a “X” failure) in tri-axial loading and unloading tests. It also observed from Table 6 that the confining pressure is higher, the damage of specimen dues to micro cracks is smaller. This can be explained that the energy stored in specimen under high confining pressure has no time to released fully when specimen failure in unloading.

#### 4.3 Simulated Damage Degree

The damage degree for the numerical model is defined by the ratio of failed contacts versus maximum number of failed

Table 6. The Damage Patterns in Loading and Unloading Tests

Confining pressures	10 MPa	20 MPa	30 MPa
Damage patterns in loading tests			
Damage patterns in unloading tests			

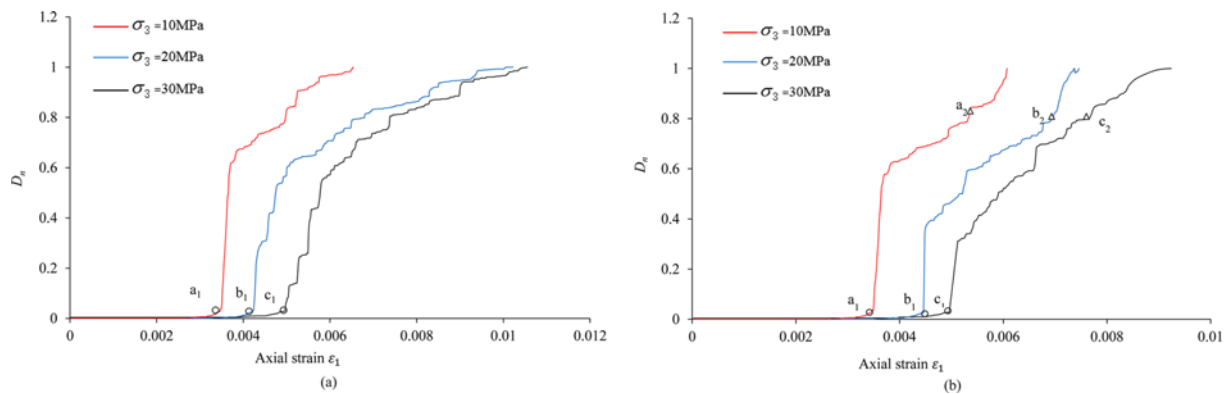


Fig. 18. The Simulation Results of Damage Degree Versus Axial Strain: (a) Loading Test, (b) Unloading Test

contacts at end of unloading:

$$D_n = \frac{N_c}{N_{c \max}} \quad (13)$$

Where  $N_c$  is the actual number of failed contacts under loading and unloading and  $N_{c \max}$  is the maximum number of failed contacts at end of unloading.

Figure 18 shows the simulation results of damage degree

versus axial strain in loading and unloading tests.  $D_n$  almost remains unchanged in the initial stage. Near the reversal of volumetric strain  $D_n$  only increases slowly. This means that near the reversal of volumetric strain micro cracks begin to form and propagate. Then  $D_n$  suddenly increases with a small increase of axial stress. It indicated that macro cracks start up due to the accumulation of micro cracks. During the process of unloading it can be seen that  $D_n$  increases steady with unloading of confining

pressures until failure of the samples.

Compare the Fig. 18(a)-(b), it clearly depicts that the rates of  $D_n$  in unloading test is faster than that in loading test. This validates the conclusion that obtained before: the damage more quickly in unloading.

The damage degrees at the reversal ( $a_1, b_1, c_1$ ) of volumetric strain are 0.03, 0.02 and 0.04. The damage degree at the start of unloading are 0.85, 0.80 and 0.78. After the reversal of volumetric strain, the axial stress sudden drop. If we neglect the influence caused by the drop, the damage degree at the start of unloading are 0.28, 0.40 and 0.45. Combined with results of lab tests, it can be concluded that although the results of damage degree are not the same,  $D_n$  is similar with  $D_E$  and  $D_W$ . In addition, under the same damage degree rock sample in higher confining pressure needs more axial stress. It indicated that confining pressure has negative effect to the damage of sample in unloading.

## 5. Conclusions

A series of conventional tri-axial compression tests was performed on specimens to investigate the damage characteristics of rocks in loading and unloading. Based energy conservation theory, the process of energy conservation was analysed. The deformation behaviour of secant modulus in loading and unloading was studied respectively. Two quantitative damage degrees defined by dissipation energy and the secant modulus respectively are introduced to evaluate the evolution of damage in the loading and unloading process. The UDEC model was used to simulate the damage evolution of rock under loading and unloading process. Based on the findings of the study, we draw the following conclusions:

1. The stress at reversal of volumetric strain increases with increasing of confining pressures.  
The failure strain for unloading is smaller than that for loading under all three confining pressures and the difference becomes more pronounced with increasing confining pressure.
2. The critical value of damage for the secant modulus increases with increasing confining pressures. In the initial stage of unloading the secant modulus decreases slowly, and finally rapidly decreases near the end of unloading which reflects the cumulative damage in the rock.
3.  $U$ ,  $U_e$  and  $U_d$  increase with increasing axial strain. The dissipation energy  $U_d$  increases with increasing confining pressure. And the rates of the dissipation energy  $U_d$  also increases with increasing confining pressure.
4.  $D_W$  and  $D_E$  increases slowly before the reversal of volumetric strain. For the same strain, lower confining pressure shows more damage. During the process of unloading,  $D_W$  increases faster. The average variations of  $D_W$  and  $D_E$  in unloading are 0.69 and 0.78, respectively. About 70%-80% of damage happened in this stage.
5. Stress-strain behavior as well as micro- and macro-mechanical damage evolution can be reproduced by the UDEC model.

## Acknowledgements

Supported by the National Natural Science Foundation of China ([51374129], [51774187]); the key research and development program of Hunan provincial science and Technology Department (2017SK2280); the key Research Foundation of Education Bureau of Hunan Province (17A184); the Innovation Team Project Plan for Prediction and Control of Uranium Mine Geotechnical Engineering Disaster of USC (NHCXTD04).

## References

- Alzo'ubi, A. K. (2012). "Modeling of rocks under direct shear loading by using discrete element method." *Alhoshn University Journal of Engineering & Applied Sciences*, Vol. 4, pp. 5-20.
- Ayling, M. R., Meredith, P. G., and Murrell, S. A. (1995). "Microcracking during triaxial deformation of porous rocks monitored by changes in rock physical properties, I." *Elastic-wave Propagation Measurements on Dry Rocks. Tectonophysics*, Vol. 245, No. 3, pp. 205-221, DOI: 10.1016/0040-1951(94)00236-3.
- Baud, P. and Meredith, P. G. (1997). "Damage accumulation during triaxial creep of Darley Dale sandstone from pore volumetry and acoustic emission." *International Journal of Rock Mechanics and Mining Sciences*, Vol. 34, No. 3, pp. 24-31, DOI: 10.1016/S1365-1609(97)00060-9.
- Bieniawski, Z. T. (1967, October). "Mechanism of brittle fracture of rock: part I—theory of the fracture process." *In International Journal of Rock Mechanics and Mining Sciences & Geomechanics Abstracts*, Vol. 4, No. 4, pp. 395IN11405-404IN12406. DOI: 10.1016/0148-9062(67)90030-7.
- Cai, M., Kaiser, P. K., Tasaka, Y., Maejima, T., Morioka, H., and Minami, M. (2004). "Generalized crack initiation and crack damage stress thresholds of brittle rock masses near underground excavations." *International Journal of Rock Mechanics and Mining Sciences*, Vol. 41, No. 5, pp. 833-847, DOI: 10.1016/j.ijrmms.2004.02.001.
- Chen, W. and Konietzky, H. (2014). "Simulation of heterogeneity, creep, damage and lifetime for loaded brittle rocks." *Tectonophysics*, Vol. 633, pp. 164-175, DOI: 10.1016/j.tecto.2014.06.033.
- Chen, W., Konietzky, H., Tan, X., and Frühwirt, T. (2016). "Pre-failure damage analysis for brittle rocks under triaxial compression." *Computers and Geotechnics*, Vol. 74, pp. 45-55, DOI: 10.1016/j.compgeo.2015.11.018.
- Christianson, M., Board, M., and Rigby, D. (2006). "UDEC simulation of triaxial testing of lithophysal tuff." *In Golden Rocks 2006, the 41st US Symposium on Rock Mechanics (USRMS)*. American Rock Mechanics Association.
- Cundall, P. A. (1980). *UDEC-A Generalised Distinct Element Program for Modelling Jointed Rock (No. PCAR-1-80)*, Cundall associates Virginia water.
- Debecker, B. and Vervoort, A. (2013). "Two-dimensional discrete element simulations of the fracture behaviour of slate." *International Journal of Rock Mechanics and Mining Sciences*, Vol. 61, pp. 161-170, DOI: 10.1016/j.ijrmms.2013.02.004.
- Dai, B., Zhao, G., Dong, L., and Yang, C. (2015). "Mechanical characteristics for rocks under different paths and unloading rates under confining pressures." *Shock and Vibration*, DOI: 10.1155/2015/578748.
- Eberhardt, E., Stead, D., Stimpson, B., and Read, R. S. (1998). "Identifying crack initiation and propagation thresholds in brittle rock." *Canadian*

- Geotechnical Journal*, Vol. 35, No. 2, pp. 222-233, DOI: 10.1139/cgj-35-2-22.
- Eberhardt, E., Stead, D., and Stimpson, B. (1999). "Quantifying progressive pre-peak brittle fracture damage in rock during uniaxial compression." *International Journal of Rock Mechanics and Mining Sciences*, Vol. 36, No. 3, pp. 361-380, DOI: 10.1016/S0148-9062(99)00019-4.
- Gang, W., Jun, S., and Wu, Z. R. (1997). "Damage mechanical analysis of unloading failure of intact rock mass under complex stress state." *Journal of Hehai University*, Vol. 25, No. 3, pp. 44-49. (in Chinese)
- Guo, Y. T., Yang, C. H., and Fu, J. J. (2012). "Experimental research on mechanical characteristics of salt rock under tri-axial unloading test." *Rock and Soil Mechanics*, Vol. 33, No. 3, pp. 725-732. (in Chinese)
- Gu, R. and Ozbay, U. (2013). *UDEC analysis of unstable rock failure in shear and compressive loading*.
- Huang, R. Q. and Huang, D. (2010). "Experimental research on affection laws of unloading rates on mechanical properties of Jinping marble under high geostress." *Chinese Journal of Rock Mechanics and Engineering*, Vol. 29, No. 1, pp. 21-33. (in Chinese)
- Huang, D. and Li, Y. (2014). "Conversion of strain energy in triaxial unloading tests on marble." *International Journal of Rock Mechanics and Mining Sciences*, Vol. 66, pp. 160-168, DOI: 10.1016/j.ijrmmms.2013.12.001.
- Lajtai, E. Z., Carter, B. J., and Duncan, E. S. (1991). "Mapping the state of fracture around cavities." *Engineering Geology*, Vol. 31, No. 3, pp. 277-289, DOI: 10.1016/0013-7952(1)90012-A.
- Li, X., Cao, W., Zhou, Z., and Zou, Y. (2014). "Influence of stress path on excavation unloading response." *Tunnelling and Underground Space Technology*, Vol. 42, pp. 237-246, DOI: 10.1016/j.tust.2014.03.002.
- Li, J., W, M. Y., Fan P. X., and Shi, C. C. (2012). "Study of loading-unloading states and energy distribution relationship for rock mass." *Rock and Soil Mechanics*, Vol. 33, No. Supp. 2, pp. 125-132. (in Chinese)
- Martino, J. B. and Chandler, N. A. (2004). "Excavation-induced damage studies at the underground research laboratory." *International Journal of Rock Mechanics and Mining Sciences*, Vol. 41, No. 8, pp. 1413-1426, DOI: 10.1016/j.ijrmmms.2004.09.010.
- Ma, M. and Brady, B. H. (1999). "Analysis of the dynamic performance of an underground excavation in jointed rock under repeated seismic loading." *Geotechnical & Geological Engineering*, Vol. 17, No. 1, pp. 1-20, DOI: 10.1023/A:1008864329747.
- Park, E. S., Martin, C. D., and Christiansson, R. (2004). "Simulation of the mechanical behavior of discontinuous rock masses using a bonded-particle model." *In Gulf Rocks 2004, the 6th North America Rock Mechanics Symposium (NARMS)*. American Rock Mechanics Association.
- Peng, R., Ju, Y., Wang, J. G., Xie, H., Gao, F., and Mao, L. (2015). "Energy dissipation and release during coal failure under conventional triaxial compression." *Rock Mechanics and Rock Engineering*, Vol. 48, No. 2, pp. 509-526, DOI: 10.1007/s00603-014-0602-0.
- Qiuling, H. A. (1998). "Loading and unloading rock masses mechanics." *Chinese Journal of Geotechnical Engineering*, Vol. 20, No. 1, pp. 114. (in Chinese)
- Qiu, S. L., Feng, X. T., Zhang, C. Q., Zhou, H., and Sun, F. (2010). "Experimental research on mechanical properties of deep-buried marble under different unloading rates of confining pressures." *Chinese Journal of Rock Mechanics and Engineering*, Vol. 29, No. 9, pp. 1807-1817. (in Chinese)
- Rellesmann, O. (1957). "Rock mechanics in regard to static loading caused by mining excavation." *In The 2nd US Symposium on Rock Mechanics (USRMS)*. American Rock Mechanics Association.
- Schmidtke, R. H. and Lajtai, E. Z. (1985). "The long-term strength of Lac du Bonnet granite." *In International Journal of Rock Mechanics and Mining Sciences & Geomechanics Abstracts*, Vol. 22, No. 6, pp. 461-465, DOI: 10.1016/0148-9062(85)90010-5.
- Shao, S., Ranjith, P. G., Wasantha, P. L. P., and Chen, B. K. (2015). "Experimental and numerical studies on the mechanical behaviour of Australian Strathbogie granite at high temperatures: An application to geothermal energy." *Geothermics*, Vol. 54, pp. 96-108, DOI: 10.1016/j.geothermics.2014.11.005.
- Sun, D. A., Matsuoka, H., Muramatsu, D., Hara, T., Kudo, A., Yoshida, Z., and Takezawa, S. (2004). "Deformation and strength characteristics of weathered soft rock using triaxial tests." *International Journal of Rock Mechanics and Mining Sciences*, Vol. 41, pp. 87-92, DOI: 10.1016/j.ijrmmms.2004.03.024.
- Tan, X., Konietzky, H., Frühwirt, T., and Dan, D. Q. (2015). "Brazilian tests on transversely isotropic rocks: Laboratory testing and numerical simulations." *Rock Mechanics and Rock Engineering*, Vol. 48, No. 4, pp. 1341-1351, DOI: 10.1007/s00603-014-0629-2.
- Tan, X. and Konietzky, H. (2014). "Numerical study of variation in Biot's coefficient with respect to microstructure of rocks." *Tectonophysics*, Vol. 610, pp. 159-171, DOI: 10.1016/j.tecto.2013.11.014.
- Thasnanipan, N., Maung, A. W., Tanseng, P., and Wei, S. H. (1998). *Performance of a braced excavation in Bangkok clay*, diaphragm wall subject to unbalanced loading conditions.
- Ulusay, R. and Hudson, J. A. ISRM (2007). *The complete ISRM suggested methods for rock characterization, testing and monitoring: 1974-2006. Commission on testing methods*, International Society of Rock Mechanics, Compilation arranged by the ISRM Turkish National Group, Ankara, Turkey.
- Wahl, M. H., McKellar, H. N., and Williams, T. M. (1997). "Patterns of nutrient loading in forested and urbanized coastal streams." *Journal of Experimental Marine Biology and Ecology*, Vol. 213, No. 1, pp. 111-131, DOI: 10.1016/S0022-0981(97)00012-9.
- Wasantha, P. L. P. and Ranjith, P. G. (2014). "Water-weakening behavior of Hawkesbury sandstone in brittle regime." *Engineering Geology*, Vol. 178, pp. 91-101, DOI: 10.1016/j.enggeo.2014.05.015.
- Wu, G. and Zhang, L. (2004). "Studying unloading failure characteristics of a rock mass using the disturbed state concept." *International Journal of Rock Mechanics and Mining Sciences*, Vol. 41, pp. 419-425, DOI: 10.1016/j.ijrmmms.2004.03.077.
- Xie, H. P., Peng, R. D., and Ju, Y. (2005). "On energy analysis of rock failure." *Chinese Journal of Rock Mechanics and Engineering*, Vol. 24, No. 15, pp. 2603-2608. (in Chinese)
- Xie, H. P., Ju, Y., Li, L. Y., and Peng, R. D. (2008). "Energy mechanism of deformation and failure of rock masses." *Chin J Rock Mech Eng.*, Vol. 27, No. 9, pp. 1729-1739. (in Chinese)
- Zhang, K., Zhou, H., Pan, P. Z., Shen, L. F., Feng, X. T., and Zhang, Y. G. (2010). "Characteristics of strength of rocks under different unloading rates." *Rock and Soil Mechanics*, Vol. 31, No. 7, pp. 2072-2078. (in Chinese)
- Zhao, X. G., Wang, J., Cai, M., Cheng, C., Ma, L., K., Su, R., Zhao, F., and Li, D. J. (2014). "Influence of unloading rate on the strain burst characteristics of Beishan granite under true triaxial unloading conditions." *Rock Mechanics and Rock Engineering*, Vol. 47, No 2, pp. 467-483, DOI: 10.1007/s00603-013-0443-2.
- Zhao, G. Y., Bing, D. A. I., Dong, L. J., and Chen, Y. A. N. G. (2015). "Energy conversion of rocks in process of unloading confining pressure under different unloading paths." *Transactions of Nonferrous Metals Society of China*, Vol. 25, No. 5, pp. 1626-1632, DOI: 10.1016/S1003-6326(15)63767-0.